Extended Quantum Anomalous Hall States in Graphene/hBN Moiré Superlattices

Zhengguang Lu[1,2]†, Tonghang Han[1]†, Yuxuan Yao[1]†, Zach Hadjri[1], Jixiang Yang[1], Junseok Seo[1], Lihan Shi[1], Shenyong Ye[1], Kenji Watanabe[3], Takashi Taniguchi[4], Long Ju[1]*

[1]Department of Physics, Massachusetts Institute of Technology, Cambridge, MA, USA.

[2] Department of Physics, Florida State University, Tallahassee, FL, 32306, USA

[3]Research Center for Electronic and Optical Materials, National Institute for Materials Science, 1-1 Namiki, Tsukuba 305-0044, Japan

[4]Research Center for Materials Nanoarchitectonics, National Institute for Materials Science, 1-1 Namiki, Tsukuba 305-0044, Japan

*Corresponding author. Email: longju@mit.edu †These authors contributed equally to this work.

Electrons in topological flat bands can form novel topological states driven by the correlation effects. The penta-layer rhombohedral graphene/hBN moiré superlattice was shown to host fractional quantum anomalous Hall effect (FQAHE) at ~400 mK[1], triggering discussions around the underlying mechanism and the role of moiré effects[2–6]. In particular, novel electron crystal states with non-trivial topology have been proposed[3,4,7–14]. Here we report electrical transport measurement in rhombohedral penta- and tetra-layer graphene/hBN moiré superlattices at electronic temperatures down to < 40 mK. We observed two more FQAH states and smaller R_{xx} values in the penta-layer devices than previously reported. In a new tetra-layer device, we observed FQAHE at moiré filling factors $v = 3/5$ and $2/3$. With a small current at the base temperature, we observed a new extended quantum anomalous Hall (EQAH) state and magnetic hysteresis, where $R_{xy} = h/e^2$ and vanishing R_{xx} span a wide range of v from 0.5 to up to 1.3. At increased temperature or current, EQAH states disappear and partially transitions into the FQAH liquid[15–17]. Furthermore, we observed displacement field-induced quantum phase transitions from the EQAH states to Fermi liquid, FQAH liquid and the likely composite Fermi liquid. Our observations establish a new topological phase of electrons with quantized Hall resistance at zero magnetic field and enrich the emergent quantum phenomena in materials with topological flat bands.

Flat electronic bands with quantum geometry have been a rich platform to explore emergent quantum phenomena driven by intertwined correlation and topology effects. In heterostructures of two-dimensional materials, such bands can be engineered with great flexibilities in structures and tuned *in situ* through dual-gating. In rhombohedral graphene (RG), gate-tunable topological flat bands stem from the highly ordered crystalline structure and additional proximity effects from neighboring layers. In particular, the penta-layer RG/hBN moiré superlattice was shown to host the fractional quantum anomalous Hall effect (FQAHE)[18,19] with six fractional states[1]. The underlying mechanism of integer and fractional QAHE in this system, however, is under debate[2–6]. This is due to the weak moiré potential experienced by electrons when exhibiting FQAHE, and the lack of an isolated moiré miniband in the single-particle picture. These puzzles, along with the high temperature scale of FQAHE and the highly tunable band structures make RG an ideal material platform to explore other emergent quantum phenomena. Some theoretical works on this system suggested a quantum anomalous Hall crystal (QAHC) that could exist under a zero or weak moiré potential[3,4,10–14], which is yet to be experimentally tested.

Here we report the electrical transport properties of the RG/hBN moiré superlattices at electronic temperatures down to < 40 mK. Information of the devices is shown in Extended Data Figure 4. In Device 1&2 (penta-layer graphene), we observed smaller R_{xx} at fractional fillings and two more FQAH states than previously reported[1]. In Device 3 (tetra-layer graphene), we observed two FQAH states. At the base temperatures and certain ranges of gate-displacement field D, surprisingly, we observed quantized anomalous Hall resistance $R_{xy} = h/e^2$ in a wide range of moiré filling factor ν accompanied by vanishing longitudinal resistance R_{xx}. These states realize the integer QAHE[1,18–20] in an extended range of ν (thus named EQAH states). At increased temperature or bias current, EQAH states are broken down. We will discuss the nature of this new topological state in comparison to QAHC and re-entrant quantum Hall insulator.

FQAHE in Penta- and Tetra-layer Graphene

Figure 1a shows schematics of devices, in which FQAHE is observed when electrons are polarized away from the moiré superlattice. With improved filters, a much lower electronic temperature than previously used[1] is realized now (see Methods). Figure 1b shows R_{xy} and R_{xx} in Device 1 at $B = 0$ T at temperature $T = 0.3$, 0.2, 0.1 and 0.01 K. Quantized $R_{xy} = h/\nu e^2$ and dips in R_{xx} can be seen at $\nu = 2/5$, 3/7, 4/9, 4/7 and 3/5 as reported previously[1], while new plateaus and dips can be identified at $\nu = 5/11$ and 5/9 below 100 mK. FQAHE persists to 10 mK at all these seven fractional fillings. The R_{xx} at fractional fillings and the neighborhood of $\nu = ½$ are all lower than reported in previously[1]. In addition, R_{xx} in Device 2 is several times smaller than in Device 1, with $R_{xx} \sim 600$ Ohm at $\nu = 3/5$ (see Extended Data Figure 9).

Figure 1d shows data from a new tetra-layer graphene/hBN moiré superlattice (Device 3) at 0.3 K. Plateaus in R_{xy} and dips in R_{xx} are clearly seen at $\nu = 3/5$, 2/3 and 1. The R_{xx} and R_{xy} maps, and the Landau fan data of Device 3 are included as Extended Data Figures 10-12.

Figure 1c demonstrates the FQAHE in Device 3. Although the graphene layer number is different, the general phase diagram is similar to that of the penta-layer devices (see Ref.[1] and Extended Data Figure 9). This observation agrees with theoretical calculations[2–4,6], and indicates RG/hBN moiré superlattice as a family of FQAHE materials. We note that the twist angles are slightly different in Device 1&2 (~0.77 deg) and Device 3 (~0.55 deg), resulting in different charge densities corresponding to $v = 1$. This difference, among other possible factors such as the band dispersion, quantum geometry, and Berry curvatures, might explain the different number of fractional states observed in tetra- and penta-layer devices.

Extended Quantum Anomalous Hall States

Figure 2 shows data from Device 1 in a large v-D range. Three regions with vanishing R_{xx} and non-zero anomalous R_{xy} are identified in Fig. 2a&b: Region 1 has a diamond shape centered at $v = 1/2$[14]; Region 2 covers $v = 0.55$ to 0.9; Region 3 covers $v = 0.93$ to 1.03. These regions compose a big anomalous Hall region, sandwiching the FQAHE region together with the very insulating (and likely Wigner crystal[1]) region at low v and D. Figure 2c&d reveal the temperature-dependence along dashed lines in Fig. 2a&b, which cut through Region 1-3. At the base temperature of 10 mK (mixing chamber temperature), R_{xx} almost vanishes at all filling factors from 1/2 to 1. Simultaneously, R_{xy} shows a wide plateau at h/e^2 except for small gaps. When T is increased, R_{xx} and R_{xy} deviate from these quantized values and recover to those reported previously at higher electronic temperatures[1].

In Device 3, we observed regions with quantized R_{xy} and vanishing R_{xx} similar to those shown in Fig. 2. There are two differences between the tetra-layer and penta-layer devices though: 1. In tetra-layer device, Region 2&3 with $R_{xy} = h/e^2$ are merged into one region; 2. The quantized $R_{xy} = h/e^2$ state extends significantly beyond $v = 1$ and reaches $v = 1.3$.

The observation of $R_{xy} = h/e^2$ and vanishing R_{xx} across a wide range of v (0.5 to 1 for penta-layer graphene, 0.5 to 1.3 for tetra-layer graphene) clearly goes beyond the IQAHE and FQAHE physics picture[1,18–20]. We name these states as extended quantum anomalous Hall (EQAH) states. At $v = 3/5$ and 2/3 and certain ranges of D, FQAH states are replaced by the EQAH states in all three devices, suggesting the latter to be the true ground state at low enough temperatures for these (v, D) combinations in Region 2. Even for Region 3 that includes $v = 1$, the R_{xy} plateau in Fig. 2d is twice wider at 10 mK than at 380 mK. The quantization of R_{xy} and R_{xx} at $v = 0.5$ to 1.3 suggests the EQAH state as a universal feature not necessarily related to the underlying moiré superlattice. Even for the smallest Region 1, it covers a much broader range of v than any FQAH state covers.

Figure 2e&f show the magnetic hysteresis of R_{xx} and R_{xy} at 10 mK at two representative (v, D) combinations in Region 2&3. Both states show $R_{xy} = \pm h/e^2$ at saturation. Together with data in Fig. 2a-d, we conclude that the EQAH state is a new topological state that realizes integer QAHE[20].

Current-Induced Break-down of EQAH State

Figure 3 shows the behavior of EQAH states under varied current excitations. We apply a DC current I_{DC} plus a 50 pA AC current to measure differential resistances. Figure 3a&b show data at the dashed lines in Figure. 2a&b at 10 mK. By increasing I_{DC} from 0 to 2.3 nA, the wide plateaus of R_{xy} = h/e^2 and R_{xx} = 0 gradually disappear and eventually evolve into shapes that are similar to the curves at 380 mK in Fig. 2c&d and in our previous work[1].

Phenomenologically, increasing I_{DC} weakens the EQAH states as increasing T does. At I_{DC} = 2.3 nA, both R_{xy} and R_{xx} curves mimic those in Fig. 2c&d at high Ts, and R_{xy} recovers to the FQAHE values at ν = 3/5 and 2/3. These observations suggest that the EQAH ground states is broken-down and replaced by the FQAH liquids[15–17] under high current excitations.

There are also differences between increasing T and I_{DC}. In Figure 2c, R_{xx} increases almost monotonically as T increases at all ν. In Figure 3b, however, R_{xx} first increases then decreases as I_{DC} increases. This non-monotonic trend is most obvious at ν = 0.6-0.8. Such non-monotonic dependence on I_{DC} is also seen for R_{xy} in Fig. 3a. We highlight such non-monotonic behaviors at two representative EQAH states, as shown in Fig. 3c-f. The first state is in Region 2 while the second state is in the Region 1. In both cases, R_{xx} remains zero at small current and shows a peak at critical current. Correspondingly, R_{xy} exhibits the quantized value of h/e^2 at small current and sudden changes at the same critical current as in the R_{xx} curve. Such threshold behaviors disappear at high temperatures, where both R_{xy} and R_{xx} remain constant.

Such threshold behaviors of differential resistances indicate non-linear voltage-current relations and are reminiscent of two other well-known correlated electron ground states. Firstly, Fig. 3d resembles the differential resistance behavior in an s-wave superconductor: R_{xx} remains zero until current hits a critical value, and a resistance peak emerges. In EQAH states, the current is carried by the chiral edge states until reaching a critical value and the bulk transport starts to contribute. Secondly, such threshold behaviors are also reminiscent of Chern insulators that exhibit integer QAHE[21–24]. In Chern insulators, the insulating bulk breaks down at high current/voltage and becomes a Fermi liquid. Quantitatively, however, the break-down of Chern insulator and EQAH states are quite different. In Device 3, the threshold currents are different by 50 times in EQAH states and in the Chern insulator at ν = 1 (see Extended Data Figure 12)—suggesting a different break-down mechanism of EQAH states from previously reported for Chern insulators[22,23].

D-Induced Phase Transitions

The displacement field provides an important tuning knob of the flat band physics in RG. With a small change of D, one can fine-tune the band structure to influence the competition between ground states that are close in energy. Figure 4a&b show T-dependent R_{xy} and R_{xx} as functions of D respectively. At around D/ε_0 = 0.92 V/nm, R_{xy} is 2h/e^2, which is compatible with the composite

Fermi liquid (CFL) picture. At high Ts, R_{xy} decreases gradually while R_{xx} changes non-monotonically from 0.9 to 0.94 V/nm. At low temperature, a plateau at R_{xy} = h/e^2 and R_{xx} = 0 emerges at intermediate Ds. This observation is consistent with the EQAH region 1 at low temperatures, and indicates quantum phase transitions from the CFL to the EQAH state to the valley-polarized Fermi liquid (FL) triggered by D.

Figure 4c&d show I_{DC}-dependent resistances as functions of D. Again, the plateaus at R_{xy} = h/e^2 and R_{xx} = 0 emerge at intermediate D only when the I_{DC} is small. Such dependence of the differential resistances on current does not happen to the CFL, as can be seen in Fig. 4e&f, where both R_{xy} and R_{xx} are constants regardless of the temperature. In contrast, in the range of D corresponding to the EQAH state, the break-down happens only at low temperature but not high temperature, as shown in Fig. 4g&h. The differences in response to T and I_{DC} clearly mark the different nature of CFL and EQAH states.

At some fractional fillings where FQAHE were observed, D can also induce quantum phase transitions. This is shown in Fig. 4i-n, in which v is fixed at 3/5, 4/7, 5/9, respectively[25]. At the base temperature, FQAH state and EQAH state each occupies a range of D, as evidenced by the plateaus at R_{xy} = h/ve^2 and R_{xy} = h/e^2. At elevated temperature, the EQAH states disappear. They become FQAH states or the transition region between FQAH states and FL states, depending on the specific v, D and T. Further tuning of D induces phase transitions to FL or Wigner crystals at the high and low ends of D, respectively. The D induced phase transitions data for all the observed fractional states are included as Extended Data Figure 8.

Discussion

Our observation of quantized R_{xy} and vanishing R_{xx} in a wide range of v at zero magnetic field, the temperature dependences of resistances, and the strong threshold behavior in transport indicate that EQAH state is a new topological phase of correlated electrons. Here we discuss two possible underlying pictures.

In picture 1, what is observed could be similar to QAHC proposed recently[3,4,11,12]. QAHC breaks the time-reversal and translational symmetries spontaneously and simultaneously in the absence of moiré effect. The EQAH state prevails in a wide range of v that is mostly in-commensurate with the moiré superlattice. This is distinct from the generalized Wigner crystal which only happens when commensurate with moiré[26,27]. Therefore, the role of moiré in the formation of EQAH states is likely different from that in generalized Wigner crystals. It is possible that the weak but non-zero moiré potential could stabilize QAHC by modulating the band structure and Berry curvature distribution. An ideal experiment to test the QAHC picture is to measure devices without moiré (when the twist angle with hBN is large). In this experiment, it is likely that even lower electronic temperatures, smaller bias current, and the right density of impurities (to pin the electron crystal as in the case of Wigner crystals) will be needed. These conditions are to be carefully engineered in future experiments.

In picture 2, the EQAH state could be similar to the re-entrant quantum Hall effect (RQHE) state happening at high magnetic fields[28–34]. The RQHE can be generally understood as the superposition of an integer quantum Hall liquid[17] and a Wigner crystal formed by the excess charges. In analogy, the integer QAHE in EQAH states can be contributed by a QAH liquid at $v = 1$ and a Wigner crystal that contributes a topologically trivial background. Although the mechanism of the QAHE at $v = 1$ remains unclear in RG/hBN, moiré effect is needed for the formation of the QAH liquid and EQAH states. We note that RQHE happens predominantly in high-index Landau levels (with rare exceptions[29,33]), while EQAH states happen mostly in the lowest moiré band. We also note that fractional quantum Hall states could be replaced at extremely low temperature due to the competition with the Wigner crystal[35–37], like FQAH states being replaced by EQAH state in our experiment.

In either case, the EQAH state is distinct from other experimentally observed topological states so far: 1. It happens at zero magnetic field and is thus different from all quantum Hall states; 2. It happens in a wide range of v and is thus different from all Chern insulators at specific charge densities. Both the pictures above and the threshold behavior of electrical transport suggest an underlying electron crystal in the EQAH state. In two dimensions, topologically trivial electron crystals have been realized with large effective mass[38–41], under high magnetic fields[42–46], and moiré superlattices or another layer hosting electrons[26,27]. A topological state containing an electron crystal at zero magnetic field, however, has never been observed. Further experiments are needed to test the possible electron crystal nature of EQAH states, through measuring the lattice in real space[41,46], diffraction peaks in momentum space[47], or narrow-band noise[48–50]. These measurements require advanced device engineering, low electronic temperature, and novel microscopy techniques, which are beyond the scope of this work. In the meanwhile, our experiment opens up opportunities to study QAHC, an un-precedented topological state of matter.

References

1. Lu, Z. *et al.* Fractional quantum anomalous Hall effect in multilayer graphene. *Nature* **626**, 759–764 (2024).
2. Dong, Z., Patri, A. S. & Senthil, T. Theory of quantum anomalous Hall phases in pentalayer rhombohedral graphene moiré structures. *ArXiv* 2311.03445 (2023).
3. Zhou, B., Yang, H. & Zhang, Y.-H. Fractional quantum anomalous Hall effects in rhombohedral multilayer graphene in the moiréless limit and in Coulomb imprinted superlattice. *ArXiv* 2311.04217 (2023).

4. Dong, J. *et al.* Anomalous Hall Crystals in Rhombohedral Multilayer Graphene I: Interaction-Driven Chern Bands and Fractional Quantum Hall States at Zero Magnetic Field. *ArXiv* 2311.05568 (2023).

5. Guo, Z., Lu, X., Xie, B. & Liu, J. Theory of fractional Chern insulator states in pentalayer graphene moiré superlattice. *Phys Rev B* **110**, 075109 (2023).

6. Kwan, Y. H. *et al.* Moiré Fractional Chern Insulators III: Hartree-Fock Phase Diagram, Magic Angle Regime for Chern Insulator States, the Role of the Moiré Potential and Goldstone Gaps in Rhombohedral Graphene Superlattices. *ArXiv* 2312.11617 (2023).

7. Halperin, B. I., s šanovi c ć, Z. & Axel, F. Compatibility of Crystalline Order and the Quantized Hall Effect. *Phys Rev Lett* **57**, 922 (1986).

8. Tešanović, Z., Axel, F. & Halperin, B. I. ``Hall crystal'' versus Wigner crystal. *Phys Rev B* **39**, 8525–8551 (1989).

9. Kivelson, S., Kallin, C., Arovas, D. P. & Schrieffer, J. R. Cooperative ring exchange and the fractional quantum Hall effect. *Phys Rev B* **36**, 1620–1646 (1987).

10. Zeng, Y., Guerci, D., Crépel, V., Millis, A. J. & Cano, J. Sublattice Structure and Topology in Spontaneously Crystallized Electronic States. *Phys Rev Lett* **132**, 236601 (2024).

11. Soejima, T. *et al.* Anomalous Hall Crystals in Rhombohedral Multilayer Graphene II: General Mechanism and a Minimal Model. *ArXiv* 2403.05522 (2024).

12. Dong, Z., Patri, A. S. & Senthil, T. Stability of Anomalous Hall Crystals in multilayer rhombohedral graphene. *ArXiv* 2403.07873 (2024).

13. Tan, T. & Devakul, T. Parent Berry curvature and the ideal anomalous Hall crystal. *ArXiv* 2403.04196 (2024).

14. Sheng, D. N., Reddy, A. P., Abouelkomsan, A., Bergholtz, E. J. & Fu, L. Quantum Anomalous Hall Crystal at Fractional Filling of Moiré Superlattices. *Phys Rev Lett* **133**, 66601 (2024).

15. Laughlin, R. B. Anomalous Quantum Hall Effect: An Incompressible Quantum Fluid with Fractionally Charged Excitations. *Phys Rev Lett* **50**, 1395–1398 (1983).

16. Eisenstein, J. P. & Stormer, H. L. The Fractional Quantum Hall Effect. *Science* **248**, 1510–1516 (1990).

17. Kivelson, S., Lee, D.-H. & Zhang, S.-C. Global phase diagram in the quantum Hall effect. *Phys Rev B* **46**, 2223–2238 (1992).

18. Park, H. *et al.* Observation of fractionally quantized anomalous Hall effect. *Nature* **622**, 74–79 (2023).

19. Xu, F. *et al.* Observation of Integer and Fractional Quantum Anomalous Hall Effects in Twisted Bilayer $MoTe_2$. *Phys Rev X* **13**, 31037 (2023).

20. Chang, C.-Z. *et al.* Experimental Observation of the Quantum Anomalous Hall Effect in a Magnetic Topological Insulator. *Science* **340**, 167–170 (2013).

21. Komiyama, S. & Kawaguchi, Y. Heat instability of quantum Hall conductors. *Phys Rev B* **61**, 2014–2027 (2000).

22. Fox, E. J. *et al.* Part-per-million quantization and current-induced breakdown of the quantum anomalous Hall effect. *Phys Rev B* **98**, 75145 (2018).

23. Kawamura, M. *et al.* Current-Driven Instability of the Quantum Anomalous Hall Effect in Ferromagnetic Topological Insulators. *Phys Rev Lett* **119**, 16803 (2017).

24. G Eber, K von Klitzing, K Ploog & G Weinmann. Two-dimensional magneto-quantum transport on GaAs-AlxGa1-xAs heterostructures under non-ohmic conditions. *Journal of Physics C: Solid State Physics* **16**, 5441 (1983).

25. Song, X.-Y., Jian, C.-M., Fu, L. & Xu, C. Intertwined fractional quantum anomalous Hall states and charge density waves. *Phys Rev B* **109**, 115116 (2024).

26. Xu, Y. *et al.* Correlated insulating states at fractional fillings of moiré superlattices. *Nature* **587**, 214–218 (2020).

27. Regan, E. C. *et al.* Mott and generalized Wigner crystal states in WSe_2/WS_2 moiré superlattices. *Nature* **579**, 359–363 (2020).

28. Xia, J. S. *et al.* Electron Correlation in the Second Landau Level: A Competition Between Many Nearly Degenerate Quantum Phases. *Phys Rev Lett* **93**, 176809 (2004).

29. Liu, Y. *et al.* Observation of Reentrant Integer Quantum Hall States in the Lowest Landau Level. *Phys Rev Lett* **109**, 36801 (2012).

30. Eisenstein, J. P., Cooper, K. B., Pfeiffer, L. N. & West, K. W. Insulating and Fractional Quantum Hall States in the First Excited Landau Level. *Phys Rev Lett* **88**, 76801 (2002).

31. Deng, N. *et al.* Collective Nature of the Reentrant Integer Quantum Hall States in the Second Landau Level. *Phys Rev Lett* **108**, 86803 (2012).

32. Chen, S. *et al.* Competing Fractional Quantum Hall and Electron Solid Phases in Graphene. *Phys Rev Lett* **122**, 26802 (2019).

33. Zhou, H., Polshyn, H., Taniguchi, T., Watanabe, K. & Young, A. F. Solids of quantum Hall skyrmions in graphene. *Nat Phys* **16**, 154–158 (2020).

34. Kumar, A., Csáthy, G. A., Manfra, M. J., Pfeiffer, L. N. & West, K. W. Nonconventional Odd-Denominator Fractional Quantum Hall States in the Second Landau Level. *Phys Rev Lett* **105**, 246808 (2010).

35. Pan, W. *et al.* Transition from an Electron Solid to the Sequence of Fractional Quantum Hall States at Very Low Landau Level Filling Factor. *Phys Rev Lett* **88**, 176802 (2002).

36. Lam, P. K. & Girvin, S. M. Liquid-solid transition and the fractional quantum-Hall effect. *Phys Rev B* **30**, 473–475 (1984).

37. Levesque, D., Weis, J. J. & MacDonald, A. H. Crystallization of the incompressible quantum-fluid state of a two-dimensional electron gas in a strong magnetic field. *Phys Rev B* **30**, 1056–1058 (1984).

38. Zhou, Y. *et al.* Bilayer Wigner crystals in a transition metal dichalcogenide heterostructure. *Nature* **595**, 48–52 (2021).

39. Smoleński, T. *et al.* Signatures of Wigner crystal of electrons in a monolayer semiconductor. *Nature* **595**, 53–57 (2021).

40. Falson, J. *et al.* Competing correlated states around the zero-field Wigner crystallization transition of electrons in two dimensions. *Nat Mater* **21**, 311–316 (2022).

41. Xiang, Z. *et al.* Quantum Melting of a Disordered Wigner Solid. *ArXiv* 2402.05456 (2024).

42. Grimes, C. C. & Adams, G. Evidence for a Liquid-to-Crystal Phase Transition in a Classical, Two-Dimensional Sheet of Electrons. *Phys Rev Lett* **42**, 795–798 (1979).

43. Andrei, E. Y. *et al.* Observation of a Magnetically Induced Wigner Solid. *Phys Rev Lett* **60**, 2765–2768 (1988).

44. Jiang, H. W. *et al.* Quantum liquid versus electron solid around ν=1/5 Landau-level filling. *Phys Rev Lett* **65**, 633–636 (1990).

45. Santos, M. B. *et al.* Observation of a reentrant insulating phase near the 1/3 fractional quantum Hall liquid in a two-dimensional hole system. *Phys Rev Lett* **68**, 1188–1191 (1992).

46. Tsui, Y.-C. *et al.* Direct observation of a magnetic-field-induced Wigner crystal. *Nature* **628**, 287–292 (2024).

47. Kakiuchi, T., Wakabayashi, Y., Sawa, H., Itou, T. & Kanoda, K. Wigner Crystallization in (DI - DCNQI)$_2$ Ag Detected by Synchrotron Radiation X-Ray Diffraction. *Phys Rev Lett* **98**, 66402 (2007).

48. Cooper, K. B., Eisenstein, J. P., Pfeiffer, L. N. & West, K. W. Observation of Narrow-Band Noise Accompanying the Breakdown of Insulating States in High Landau Levels. *Phys Rev Lett* **90**, 226803 (2003).

49. Chen, Y. P. *et al.* Evidence for Two Different Solid Phases of Two-Dimensional Electrons in High Magnetic Fields. *Phys Rev Lett* **93**, 206805 (2004).

50. Madathil, P. T. *et al.* Moving Crystal Phases of a Quantum Wigner Solid in an Ultra-High-Quality 2D Electron System. *Phys Rev Lett* **131**, 236501 (2023).

Main Figure Legends

Figure 1. Fractional quantum anomalous Hall effects in rhombohedral penta- and tetra-layer graphene/hBN moiré superlattice devices. a. *Schematic of the device configuration and measurement conditions. In both penta- and tetra-layer devices, electrons are polarized to the layer that is furthest from the moiré superlattice when the FQAHE is observed.* ***b.*** *Temperature-dependent R_{xy} (upper panel) and R_{xx} (lower panel) of Device 1, the penta-layer device, taken at $D/\varepsilon_0 = 0.928$ V/nm. Clear plateaus in R_{xy} and dips in R_{xx} can be seen at $\nu = 2/5, 3/7, 4/9, 4/7$ and $3/5$ as reported previously, while new fractional states can be identified at $\nu = 5/11$, and $5/9$ at the lowest temperature. At a fixed ν corresponding to the FQAH state, R_{xx} decreases as the temperature is lowered.* ***c.*** *R_{xx} and R_{xy} in the tetra-layer device at 300 mK and taken at $D/\varepsilon_0 = 0.957$ V/nm. Quantized R_{xy} and dips in R_{xx} can be seen at $\nu = 3/5$ and $2/3$—underscoring the universal FQAHE phenomena in rhombohedral graphene/hBN moiré superlattice system. All data are extracted by symmetrizing and anti-symmetrizing data taken at out-of-plane magnetic fields $B = \pm 0.1$ T.*

Figure 2. Extended quantum anomalous Hall states in Device 1 the penta-layer device. a&b. *Mapping of R_{xx} and R_{xy} in a large range of ν and D at a mixing chamber temperature of 10 mK. Three regions (labeled by numbers and arrows) show quantized R_{xy} at $h/e^2$and vanishing R_{xx}, located at around $\nu = 1/2$, spanning between $\nu = 0.55$ and 0.83, as well as around $\nu = 1$. These three regions are almost connected into one big region with $R_{xy} = h/e^2$ that swamps the FQAH states at $\nu > 1/2$. The dashed lines correspond to $D/\varepsilon_0 = 0.946$ V/nm.* ***c&d.*** *Temperature-dependent R_{xx} and R_{xy} taken along the dashed line in a&b. From high temperature to low temperature, R_{xx} decreases and the dips corresponding to FQAH states at $\nu = 3/5$ and $2/3$ become small bumps, while the R_{xy} approaches h/e^2 from values both below and above it. The plateau of R_{xy} at h/e^2 spans almost from $\nu = 1/2$ to 1 at 10 mK, and the gap at $\nu = 0.94$ and 0.53 are on the trend of being closed as the temperature is lowered.* ***e&f.*** *Magnetic hysteresis scans of R_{xx} and R_{xy} at $(\nu,) = (0.719, 0.928$ V/nm) and (0.5, 0.946 V/nm) respectively at 10 mK, featuring quantized $R_{xy} = h/e^2$ in both cases. All data are extracted by symmetrizing/anti-symmetrizing data taken at $B = \pm 0.1$ T.*

Figure 3. Break-down of EQAH states in Device 1 the penta-layer graphene/hBN device. a&b. *Differential resistance R_{xx} and R_{xy} taken at the dashed lines in Fig. 2a&b at 10 mK, using an AC current of 50 pA on top of a varied DC current. The quantized $R_{xy} = h/e^2$ and vanishing R_{xx} can be seen at small DC current, while the high-temperature behavior (including FQAHE at $\nu = 3/5$ and $2/3$) as shown in Fig. 2 is qualitatively reproduced at $I_{DC} = 2.3$ nA. This suggests that the EQAH state is the true ground state at this ν in certain range of D, while the fractional quantum Hall liquid can be recovered by a large DC current. Non-monotonic dependence of R_{xx} on I_{DC}, however, can be seen at intermediate I_{DC}. This is clearly different from the monotonic dependence of R_{xx} on the temperature, as shown in Fig. 2c.* ***c&d.*** *Current-dependent R_{xx} and R_{xy} taken at $(\nu, D/) = (0.74, 0.948$ V/nm) and varying temperatures, revealing the quantized transport at small current in the EQAH state, and the anomalous quantum Hall liquid transport at high current when the EQAH state is broken down. The pair of peaks in R_{xx} at the break-down threshold corresponds to the non-*

monotonic dependence of R_{xx} on I_{DC} in ***b****, and is reminiscent of s-wave superconductors and Chern insulators to some extent.* ***e&f.*** *Current-dependent R_{xx} and R_{xy} taken at (ν, D/) = (0.5, 0.951 V/nm) and varying temperatures, showing similar behaviors as in* ***c&d****.*

Figure 4. Phase transitions from the EQAH states to (composite) Fermi liquid and FQAH liquid. a&b. *R_{xy} and R_{xx} at $\nu = 1/2$ and varying D across a range of temperatures. The plateaus at $R_{xy} = 2h/e^2$ and h/e^2 that correspond to CFL and EQAH can be clearly seen at low temperatures. At very high D, the transport behavior aligns with a valley-polarized Fermi-liquid. At very low D, the resistance diverges and suggests a Wigner crystal state.* ***c&d.*** *Differential resistances R_{xy} and R_{xx} taken at $\nu = 1/2$ and varying D at 10 mK, using an AC current of 50 pA on top of a DC current. Behaviors in different ranges of D qualitatively agree with that in* ***a&b****.* ***e&f.*** *Current dependence of differential resistances R_{xy} and R_{xx} at (ν, D/) = (0.5, 0.921 V/nm), agreeing with the linear voltage-current transport of CFL.* ***g&h.*** *Current dependence of differential resistances R_{xy} and R_{xx} at (ν, D/) = (0.5, 0.946 V/nm), revealing the linear voltage-current transport behavior at high temperatures when the EQAH state is broken-down to fractional quantum Hall liquid, which is contrasted by the non-linear voltage-current transport when the EQAH is un-perturbed at low temperatures.* ***i-n.*** *Dependence of R_{xy} and R_{xx} on D at 10 mK, taken at ν = 3/5, 4/7 and 5/9 respectively. Plateaus corresponding to FQAH and EQAH states are clearly seen and connected by phase transitions induced by D at the same ν.*

Methods

High Through-Put Fabrication of Rhombohedral Graphene Stacks Enabled by Advanced Infrared Imaging and Device Fabrication

Device 1&2 were used in Ref. [1]where the description of device fabrication can be found. Device 3 was made in generally the same procedures as Device 1&2, except for the imaging of the rhombohedral stacking order. We developed a new infrared imaging technique based on InGaAs camera, which is installed on a regular optical microscope and can take pictures of the graphene flakes. Different stacking orders in graphene can be identified based on their different infrared conductivities and contrast with the substrate, as described in Ref[51,52]. Compared to the near field infrared nanoscopy technique we employed previously[53–55], the far-field imaging based on the InGaAs camera has a much higher efficiency due to the multi-pixel data collection simultaneously.

We combine the near-field[56] and far-field approaches[57], together with Raman spectroscopy[58,59] to visualize and confirm stacking orders in the exfoliated flakes and assembled stacks.

Extended Data Figure 1 shows how this imaging method is implemented. We picked up the top hBN, graphite, middle hBN, and the penta-layer graphene using polypropylene carbonate (PPC) film and landed it on a prepared bottom stack consisting of an hBN and graphite bottom gate. We used the IR camera to quickly screen the exfoliated graphene flakes and identify the rhombohedral domains. We also checked if the stacking order is preserved after picking up the graphene with hBN and after the stack is finished. The device was then etched into a Hall bar structure using standard e-beam lithography (EBL) and reactive-ion etching (RIE). We deposited Cr/Au for electrical connections to the source, drain and gate electrodes.

There are two caveats to note though, as shown in Extended Data Figure 2. Firstly, for multilayer graphene thicker than three layers, there are intermediate stacking orders other than rhombohedral and Bernal stacking. Some of the intermediate stackings show similar responses to the rhombohedral stacking on the InGaAs camera and could mislead the judgment. Near-field infrared nanoscopy works better in differentiating rhombohedral stacking from other stackings, possibly due to the longer wavelength used in the near-field measurements. Secondly, the spatial resolution of the far-field imagining is limited to ~one micron due to the diffraction limit of infrared light, and could miss domain structures with mixed stacking orders and domain walls that are smaller than the spatial resolution[60,61].

Previous Experimental Efforts on Rhombohedral Multilayer Graphene

Rhombohedral (ABC) stacked multilayer graphene system have been subject to intense theoretical[62,63] and experimental[58,64–66] studies since the early 2010s, due to their unique electronic band structure arising from their staircase-like stacking configuration. This specific stacking order leads to the formation of topological flat bands, particularly in thicker multilayers, which enhances electron-electron interactions and give rise to a rich variety of correlated electronic phases including correlated insulators[55,56,58,59,66–71], Chern insulators[55,61], orbital magnetism[70,72], multiferroicity[54] and superconductivity[73,74]. By introducing moire potential via adjacent hBN layer, rhombohedral graphene shows Mott insulators[69], tuneable ferromagnetism and Chern insulators[68], as well as superconductivity[73]. Recent studies have demonstrated that, under the application of a perpendicular electric field, multilayer rhombohedral graphene/hBN moire can host integer and fractional quantum anomalous Hall effect[1,57]. Notably, the potential co-existence of FQAHE and superconductivity in graphene systems paves the way for realizing non-Abelian anyonic braiding at zero magnetic field.

Transport Measurement

The device was measured in a Bluefors LD250 dilution refrigerator with a base electronic temperature of < 40 mK. This estimated value is obtained by measuring a similar rhombohedral graphene device that has a superconducting transition temperature of ~40 mK as shown in Extended Data Figure 3. Stanford Research Systems SR830 lock-in amplifiers were used to measure the longitudinal and Hall resistance R_{xx} and R_{xy} with an AC frequency at 17.77 Hz. The DC and AC currents are generated by Keysight 33210A function generator through a 300 MOhm resistor. Keithley 2400 source-meters were used to apply top and bottom gate voltages. Top-gate voltage V_t and bottom-gate voltage V_b are swept to adjust doping density $n_e = (C_tV_t + C_bV_b)/e$ and displacement field $D/\varepsilon_0 = (C_tV_t - C_bV_b)/2$, where C_t and C_b are top-gate and bottom-gate capacitance per area calculated from the Landau fan diagram.

Dis-Entangling Longitudinal and Hall Resistances

Devices 1&2 are the same as used in Ref.[1] and has been measured in the same way to dis-entangle the R_{xx} and R_{xy}[75]. As shown in Fig. 1c, device 3 is in a Hall bar geometry with good electric contacts on both sides of the channel at high displacement fields. We use electrodes ‘S’ & ‘D’ to pass the current, electrodes ‘1’ & ‘2’ to measure R_{xx} and electrodes ‘2’ & ‘3’ to measure R_{xy}. Measurements performed at opposite magnetic fields (larger than the coercive field) can thus be used to extract R_{xx} and R_{xy} at $B = 0$ for the IQAH, FQAH and EQAH states, following:

$$R_{xx}(0) = (R(B) + R(-B))/2 \qquad \text{and} \qquad R_{xy}(0) = (R(B) - R(-B))/2.$$

Contact Configurations in Device 1, 2 and 3

Extended Data Figure 4a shows a summary of the basic device information. Extended Data Figure 4b&c show contact configurations used in device 1, 2 and 3. Since the graphite layers being used as top and bottom gates are never perfectly overlapped, one will always suffer from p-n junction type of electrical contacts in two out of the four quadrants in the (n, D) phase space. To avoid the formation of a p-n junction in the quadrant that one is interested in, the key point is to design the size and position of the top and bottom gate. For example, we are interested in the (n, $D>0$) quadrant for the EQAH, so the design needs to make sure all contacts are free of p-n junctions in this quadrant. Our old design used in device 1 and 2 is illustrated in Extended Data Figure 4b, where the top and bottom gate graphite protrude at the opposite sides. Subsequently, in the quadrant (n, $D>0$), the part only covered by the top gate is n-doped (good contact due to the absence of a p-n junction), and the part only covered by bottom gate is p-doped (bad contact due to a p-n junction). Therefore, the Hall bar type of measurement is impossible since electrodes on one side of the Hall bar have bad electrical contacts to the graphene channel. Our new contact design used in tetra-layer device 3 is shown in Extended Data Figure 4c, where we intentionally make the top gate protrude from the back gate on both sides of the sample. In this way, all electrodes have good contact in the (n, $D>0$) quadrant. In contrast, if one is interested in measuring the (n, $D<0$) quadrant, the bottom gate should be larger than the top gate on both sides of the sample to avoid forming a p-n junction.

Definition of The Displacement Field

The definition of the displacement field direction and where the low energy electron will be polarized could be quite confusing in literature. In our definition, the displacement field is positive when it is pointing from the top gate to the bottom gate. In this case, the low-energy electronic states in conduction band (valence band) are polarized to the bottom (top) layer as illustrated in Extended Data Figure 5a. On the other hand, if the displacement field is negative, the conduction band electron will be polarized to the top layer (Extended Data Figure 5b). In other words, the electrons in the valence band will indeed accumulate towards the direction opposite to the direction of D, because they have the privilege to occupy the lower energy states. In contrast, the electrons in the conduction band are forced to take the higher energy states that are polarized towards the same direction of D. To further clarify on this common confusion, we show in Extended Data Figure 5c&d the ν-D map and the corresponding V_t-V_b map of the longitudinal resistance.

Temperature and Bias-Induced Transition from EQAH States to FQAH States

Extended Data Figure 6 shows a direct comparison between $\nu = 1/2$, 3/5 and 2/3. It can be seen that similar threshold behaviors happen to $\nu = 3/5$ and 2/3: at low temperature and small bias current, they both show an EQAH state; at higher temperature or beyond a threshold DC current, Rxy deviates from h/e^2 and shows quantized values of $h/\nu e^2$ as the device enters the FQAH states.

Evolution of The EQAH Contour versus Temperature

Extended Data Figure 7a demonstrates the EQAH region shrinking process as a contour plot. Both the Region 1&2 vanish at above 100 mK, while Region 3 shrinks and connects to the $\nu = 1$ QAH state which survives to much higher temperatures as shown in Extended Data Figure 7c-f.

EQAH States in Device 2

Extended Data Figure 9 shows data from Device 2, the other penta-layer graphene/hBN device on the same chip as Device 1. The twist angle and general phase diagram of Device 2 are similar to those of Device 1, featuring FQAHE, EQAH states and phase transitions similar to described in Fig. 1-4 in the main text. As shown in Extended Data Figure 9e, R_{xx} at fractional fillings and the neighborhood of $\nu = ½$ are several times smaller than in Device 1, with $R_{xx} \sim 600$ Ohm at $\nu = 3/5$. This is about one order of magnitude smaller than reported in Ref. [1].

FQAHE and EQAH states in Device 3

Extended Data Figure 10-12 show data from Device 3, a newly made tetra-layer rhombohedral graphene/hBN device. At 300 mK, the phase diagram shows IQAHE and FQAHE. At 10 mK, the EQAH states emerge and dominate a large range of (ν, D) from $\nu = 0.5$ to 1.3.

Methods References

Lui, C. H. *et al.* Imaging Stacking Order in Few-Layer Graphene. *Nano Lett* **11**, 164–169 (2011).

Yan, J.-A., Ruan, W. Y. & Chou, M. Y. Enhanced optical conductivity induced by surface states in ABC-stacked few-layer graphene. *Phys Rev B* **83**, 245418 (2011).

Han, T. *et al.* Large quantum anomalous Hall effect in spin-orbit proximitized rhombohedral graphene. *Science* **384**, 647–651 (2024).

Han, T. *et al.* Orbital multiferroicity in pentalayer rhombohedral graphene. *Nature* **623**, 41–47 (2023).

Han, T. *et al.* Correlated insulator and Chern insulators in pentalayer rhombohedral-stacked graphene. *Nat Nanotechnol* **19**, 181–187 (2024).

Liu, K. *et al.* Spontaneous broken-symmetry insulator and metals in tetralayer rhombohedral graphene. *Nat Nanotechnol* **19**, 188–195 (2024).

Xie, J. *et al.* Even- and Odd-denominator Fractional Quantum Anomalous Hall Effect in Graphene Moire Superlattices. *ArXiv* 2405.16944 (2024).

Bao, W. *et al.* Stacking-dependent band gap and quantum transport in trilayer graphene. *Nat Phys* **7**, 948–952 (2011).

59. Shi, Y. *et al.* Electronic phase separation in multilayer rhombohedral graphite. *Nature* **584**, 210–214 (2020).

60. Ju, L. *et al.* Topological valley transport at bilayer graphene domain walls. *Nature* **520**, 650–655 (2015).

61. Sha, Y. *et al.* Observation of a Chern insulator in crystalline ABCA-tetralayer graphene with spin-orbit coupling. *Science* **384**, 414–419 (2024).

62. Zhang, F., Sahu, B., Min, H. & MacDonald, A. H. Band structure of ABC-stacked graphene trilayers. *Phys Rev B* **82**, 35409 (2010).

63. Koshino, M. & McCann, E. Gate-induced interlayer asymmetry in ABA-stacked trilayer graphene. *Phys Rev B* **79**, 125443 (2009).

64. Zou, K., Zhang, F., Clapp, C., MacDonald, A. H. & Zhu, J. Transport Studies of Dual-Gated ABC and ABA Trilayer Graphene: Band Gap Opening and Band Structure Tuning in Very Large Perpendicular Electric Fields. *Nano Lett* **13**, 369–373 (2013).

65. Zhang, L., Zhang, Y., Camacho, J., Khodas, M. & Zaliznyak, I. The experimental observation of quantum Hall effect of l=3 chiral quasiparticles in trilayer graphene. *Nat Phys* **7**, 953–957 (2011).

66. Lee, Y. *et al.* Competition between spontaneous symmetry breaking and single-particle gaps in trilayer graphene. *Nat Commun* **5**, 5656 (2014).

67. Myhro, K. *et al.* Large tunable intrinsic gap in rhombohedral-stacked tetralayer graphene at half filling. *2d Mater* **5**, 045013 (2018).

68. Chen, G. *et al.* Tunable correlated Chern insulator and ferromagnetism in a moiré superlattice. *Nature* **579**, 56–61 (2020).

69. Chen, G. *et al.* Evidence of a gate-tunable Mott insulator in a trilayer graphene moiré superlattice. *Nat Phys* **15**, 237–241 (2019).

70. Zhou, W. *et al.* Layer-polarized ferromagnetism in rhombohedral multilayer graphene. *Nat Commun* **15**, 2597 (2024).

71. Ding, J. *et al.* Electrical switching of chirality in rhombohedral graphene Chern insulators. *ArXiv* 2406.14289 (2024).

72. Zhou, H. *et al.* Half- and quarter-metals in rhombohedral trilayer graphene. *Nature* **598**, 429–433 (2021).

73. Chen, G. *et al.* Signatures of tunable superconductivity in a trilayer graphene moiré superlattice. *Nature* **572**, 215–219 (2019).

74. Zhou, H., Xie, T., Taniguchi, T., Watanabe, K. & Young, A. F. Superconductivity in rhombohedral trilayer graphene. *Nature* **598**, 434–438 (2021).

75. Serlin, M. *et al.* Intrinsic quantized anomalous Hall effect in a moiré heterostructure. *Science* **367**, 900–903 (2020).

Acknowledgement

We acknowledge helpful discussions with T. Senthil, F. Wang, R. Ashoori and A. Young. L.J. acknowledges support from a Sloan Fellowship. T.H. acknowledges support from a Mathworks Fellowship. This work was funded by the US Department of Energy, Office of Science, Basic Energy Sciences, Materials Sciences and Engineering Division under contract no. DE-SC0025325. The device fabrication of this work was carried out at the Harvard Center for Nanoscale Systems and MIT.Nano. K.W. and T.T. acknowledge support from the JSPS KAKENHI (Grant Numbers 20H00354, 21H05233 and 23H02052) and World Premier International Research Center Initiative (WPI), MEXT, Japan.

Author Contributions

L.J. supervised the project. Z.L., T.H., and Z.H., performed the DC magneto-transport measurement. T.H., Y.Y., L.S., and S.Y. fabricated the devices. J.Y., J.S., Z.L. and T.H. helped with installing and testing the dilution refrigerator. K.W. and T.T. grew hBN crystals. All authors discussed the results and wrote the paper.

Competing Interests The authors declare no competing interests.

Data Availability The data shown in the main figures are available from https://doi.org/10.7910/DVN/YPO5VS. Other data that support the finding of this study are available from the corresponding authors upon reasonable request.

Extended Data Figure Legends

Extended Data Figure 1. Visible and infrared far-field imaging of multilayer graphene during fabrication. a. *Optical image of an exfoliated graphene flake on SiO_2/Si substrate, taken with a regular optical microscope. The majority of the flake (outlined by dashed lines) is tetra-layer. Scale bar: 20 μm. No contrast can be seen within the tetra-layer region.* ***b.*** *Infrared image of the same flake as in* ***a****, taken by an InGaAs camera. Domains with different contrasts can be seen, which correspond to different stacking orders. The rhombohedral stacking domain (ABCA) has a contrast between the Bernal stacked domain (ABAB) and an intermediate stacked domain (ABCB). These stacking orders have been confirmed by Raman scattering measurement. We cut 6 rectangles out of the ABCA domain using a laser, as outlined by dashed boxes.* ***c.*** *The InGaAs camera image of 3 (out of 6 ABCA) flakes that are picked up. The two flakes on the left have partially changed to other stacking orders, while the right-most flake remains in ABCA stacking.* ***d.*** *The InGaAs camera image of the three flakes in* ***c*** *after they are dropped down to hBN and bottom graphite gate. The right-most flake in* ***c*** *remained in the ABCA stacking, as indicated by the right arrow. It has a clear contrast with the middle flake in* ***c****. The ABCA flake in the dashed box was made into Device 3.*

Extended Data Figure 2. Comparison between far-field infrared imaging and near-field infrared imaging. a&b. *InGaAs camera image and near-field infrared nanoscopy image of an exfoliated multilayer graphene flake on* SiO_2*/Si substrate. The latter reveals more domains (labeled as 1-4) with clear contrast than the former does.* ***c&d.*** *Near-field infrared nanoscopy images of two exfoliated trilayer graphene flakes. Both images show domain and domain walls that have dimensions much smaller than 1* μ*m, which is well-below the diffraction-limit of the far-field imaging based on the InGaAs camera.*

Extended Data Figure 3. Estimation of the electron temperature. a. *Temperature dependence of* R_{xx} *in a graphene superconducting state. The density range of the superconducting dome remains expanding below 40 mK.* ***b.*** *Temperature dependence of* R_{xx} *at* $n_e = 1.9\times10^{12}$ cm^{-2}.

Extended Data Figure 4. Summary of the device and electrical contact information. a. *Basic information of the three devices. Scale bars: 3* μ*m in Devices 1&2, and 4* μ*m in Device 3.* ***b.*** *Schematics of the gates and contacts layout in device 1 and 2. Top and bottom graphite gate shifted relative to each other creating a n-p-n junction on one side of the contacts.* ***c.*** *Gates and contacts layout in device 3 with optimized geometry. No p-n junction will be formed on either side of the device.*

Extended Data Figure 5. Definition of the displacement field. a&b. *Schematics of the layer polarization of the low energy electrons in the conduction band.* ***c.*** R_{xx} *versus the filling factor* v *and displacement field* D/ϵ_0 *at the base temperature.* ***d.*** R_{xx} *versus top and bottom gate voltages at the base temperature.*

Extended Data Figure 6. Temperature-dependent differential resistance at fractional fillings. R_{xx} *and* R_{xy} *versus DC bias at* $v = 1/2$ & $D/\epsilon_0 = 0.951$ *V/nm (**a&b**),* $v = 2/3$ & $D/\epsilon_0 = 0.952$ *V/nm (**c&d**), and* $v = 3/5$ & $D/\epsilon_0 = 0.950$ *V/nm (**e&f**). In all three cases, the transition from EQAH to FQAH can be induced by increasing the temperature or the bias DC current.*

Extended Data Figure 7. EQAH state contour plots of regions with $R_{xy} = h/e^2$ ***at representative temperatures. a.*** *Temperature evolution of the EQAH Region 1-3.* ***b&c.*** *Overlapping EQAH contour plots at selective temperatures to demonstrate the shrinking of the range as the temperature increases.* ***d&e.*** *Temperature evolution of the* R_{xx} *and* R_{xy} *line cuts versus filling across* $v = 1$. ***f.*** *Temperature dependence of* R_{xx} *and* R_{xy} *at* $v = 1$ *and EQAH (*$v=0.96$*) states.*

Extended Data Figure 8. Temperature dependent R_{xy} ***versus displacement field. a.*** R_{xy} *versus displacement field at moiré filling factor 2/3. The EQAH state become FQAH as the temperature increases to about 340 mK.* ***b.*** R_{xy} *versus displacement field at moiré filling factor 3/5. At base temperature, the FQAH state occupies the displacement field range from 0.920 V/nm to 0.930 V/nm and the EQAH state occupies from 0.945 V/nm to 0.960 V/nm. As the temperature increases, EQAH in displacement field range 0.945 V/nm to 0.950 V/nm will lose the quantization at* h/e^2 *and become quantized at* $5h/3e^2$*, which indicates the recovery of FQAH at this temperature.* ***c&d.*** R_{xy}

versus displacement field at moiré filling factor ν = 4/7 and 5/9. FQAH states stays from the base temperature up to more than 400 mK in the displacement field range from 0.920 V/nm to 0.940 V/nm. The EQAH states near 0.95 V/nm become the phase boundary between FQAH at lower D side and Fermi liquid at higher D side as the temperature increases. ***e-h.*** *R_{xy} versus displacement field at moiré filling factor ν = 5/11, 4/9, 3/7 and 2/5. FQAH states persist from base temperature up to more than 400 mK in a range of displacement field. The displacement field range will shrink as the phase boundary between FQAH and Fermi liquid broadened by temperature.*

Extended Data Figure 9. Phase diagram of Device 2, a penta-layer rhombohedral graphene/hBN moiré superlattice, at I_{DC} = 0 A and I_{AC} = 0.2 nA. **a&b.** *Mapping of R_{xx} and R_{xy} in a large range of ν and D at a mixing chamber temperature of 10 mK. The main features are similar to that of Device 1 shown in Fig. 2. Three regions show quantized R_{xy} at $h/e^2$and vanishing R_{xx}, located at around ν = 1/2, spanning between ν = 0.55 and 0.83, as well as around ν = 1. These three regions are almost connected into one big region with $R_{xy} = h/e^2$ that swamps the FQAH states at ν > 1/2.* ***c.*** *Line-cut of R_{xy} at D/ε_0 = 0.96 V/nm and varied bias current, featuring a wide plateau at h/e^2.* ***d.*** *R_{xy} at ν = ½, featuring the phase transition from CFL to EQAH driven by displacement field.* ***e***. *R_{xx} and R_{xy} along the dashed lines in* ***a&b****, showing plateaus and dips of FQAHE at fractional fillings. The R_{xx} at fractional fillings and the neighborhood of ν=½ are several times smaller than in Device 1, with R_{xx} ~ 600 Ohm at ν = 3/5.*

Extended Data Figure 10. FQAHE in Device 3 at 300 mK. a&b. *Mapping of R_{xx} and R_{xy} in a large range of ν and D at I_{DC} = 0 nA and I_{AC} = 0.1 nA, which is beyond the break-down threshold current of EQAH states.* ***c.*** *Landau fan corresponding to the line-cut in* ***c****, where the dashed lines are derived from the Streda's formula for states with $R_{xy} = 5h/3e^2$, $3h/2e^2$ and h/e^2, respectively. The dispersions of dips in R_{xx} agree well with the dashed lines, as expected for fractional and integer Chern insulators at ν = 3/5, 2/3 and 1.*

Extended Data Figure 11. Phase diagram of Device 3, a tetra-layer rhombohedral graphene/hBN moiré superlattice, at 10 mK, I_{DC} = 0 A and I_{AC} = 0.2 nA. a&b. *Mapping of R_{xx} and R_{xy} in a large range of ν and D at a mixing chamber temperature of 10 mK. Different from Device 1&2, the region with quantized R_{xy} at $h/e^2$and vanishing R_{xx} shifts to higher moiré filling factors. This is likely due to the smaller twist angle and smaller charge density corresponding to ν = 1 in Device 3. As a result, Region 2&3 in Fig. 2 merge into one region without a gap in between. At the same time, the EQAH region extends significantly beyond ν = 1 and reaches ν = 1.3.*

Extended Data Figure 12. Current-induced break-down of EQAH state and Chern insulators in Device 3 at 10 mK. a. *Mapping of R_{xy} in a large range of ν and D at I_{DC} = 0 A and I_{AC} = 0.2* *nA. Five states at 'stars' positions show quantized* R_{xy} *at* h/e^2 *and vanishing* R_{xx}. ***b&c.*** R_{xx} *and* R_{xy} *as a function of* I_{DC} *at the light and dark blue 'star' positions corresponding to* $\nu = 1$ *in* ***a****, showing the break-down behavior of the C = 1 Chern insulator at large current (>50 nA).* ***d-f.*** R_{xx} *and* R_{xy} *as a function of* I_{DC} *at the green, pink and purple 'star' positions in* ***a****, showing the break-down behavior of the EQAH states at small current (< 1 nA) in contrast to the large break-down current of the C = 1 Chern insulator in* ***b&c****. Inset: zoom-in of curves at around* I_{DC} *= 0 nA, which reveal the threshold of EQAH break-down at ~ 1 nA. Note: Spike-like rapid changes in* ***b****-****f*** *are artifacts from voltage source meter when switching the output range.*

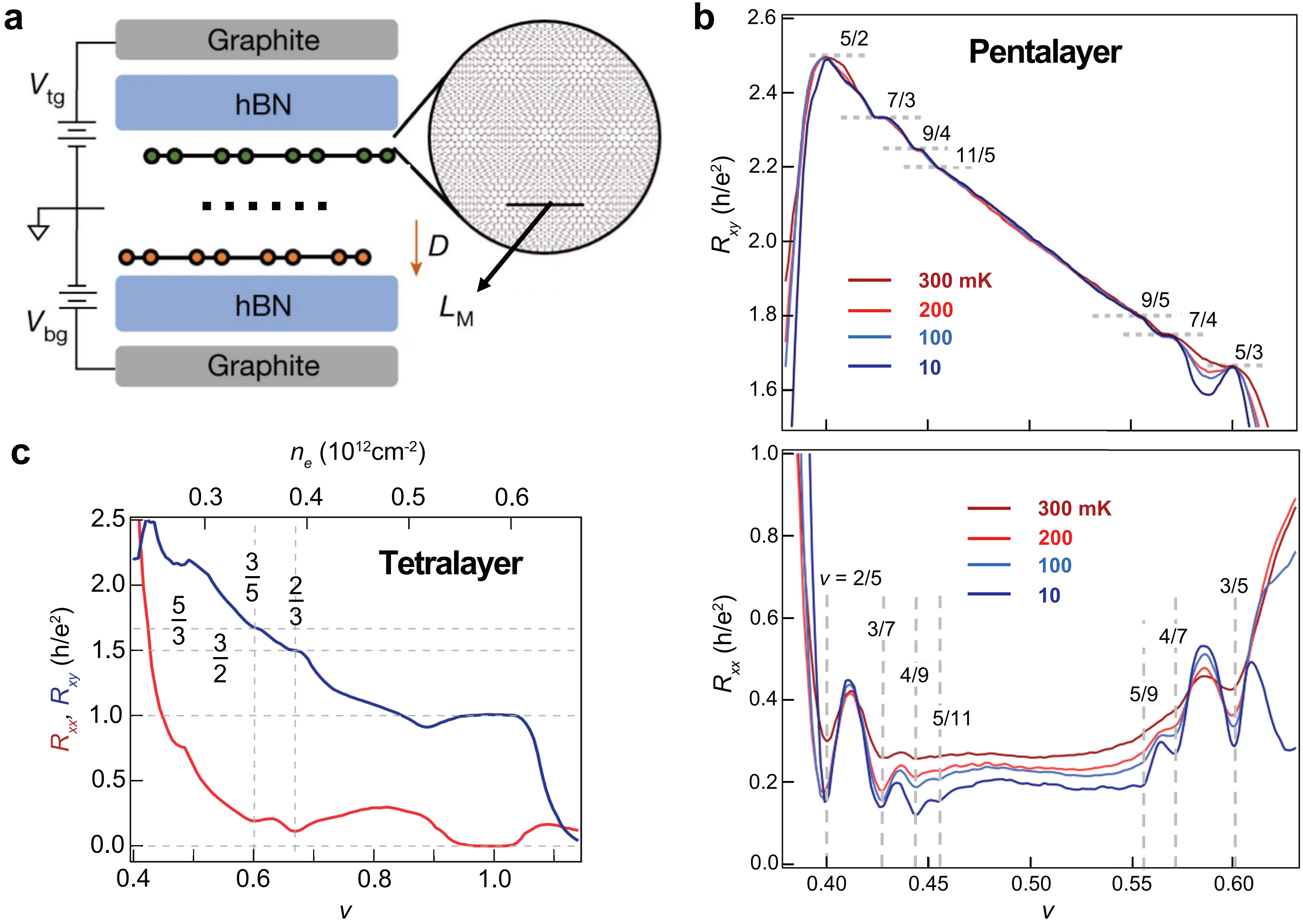
a
Graphite
hBN
hBN
Graphite
V_{tg}
V_{bg}
D
L_M
b
Pentalayer
R_{xy} (h/e^2)
2.6
2.4
2.2
2.0
1.8
1.6
5/2
7/3
9/4
11/5
9/5
7/4
5/3
300 mK
200
100
10
R_{xx} (h/e^2)
1.0
0.8
0.6
0.4
0.2
0.0
ν = 2/5
3/7
4/9
5/11
5/9
4/7
3/5
0.40
0.45
0.50
0.55
0.60
ν
c
n_e (10^{12}cm^{-2})
0.3
0.4
0.5
0.6
Tetralayer
R_{xx}, R_{xy} (h/e^2)
2.5
2.0
1.5
1.0
0.5
0.0
5/3
3/2
3/5
2/3
0.4
0.6
0.8
1.0
ν

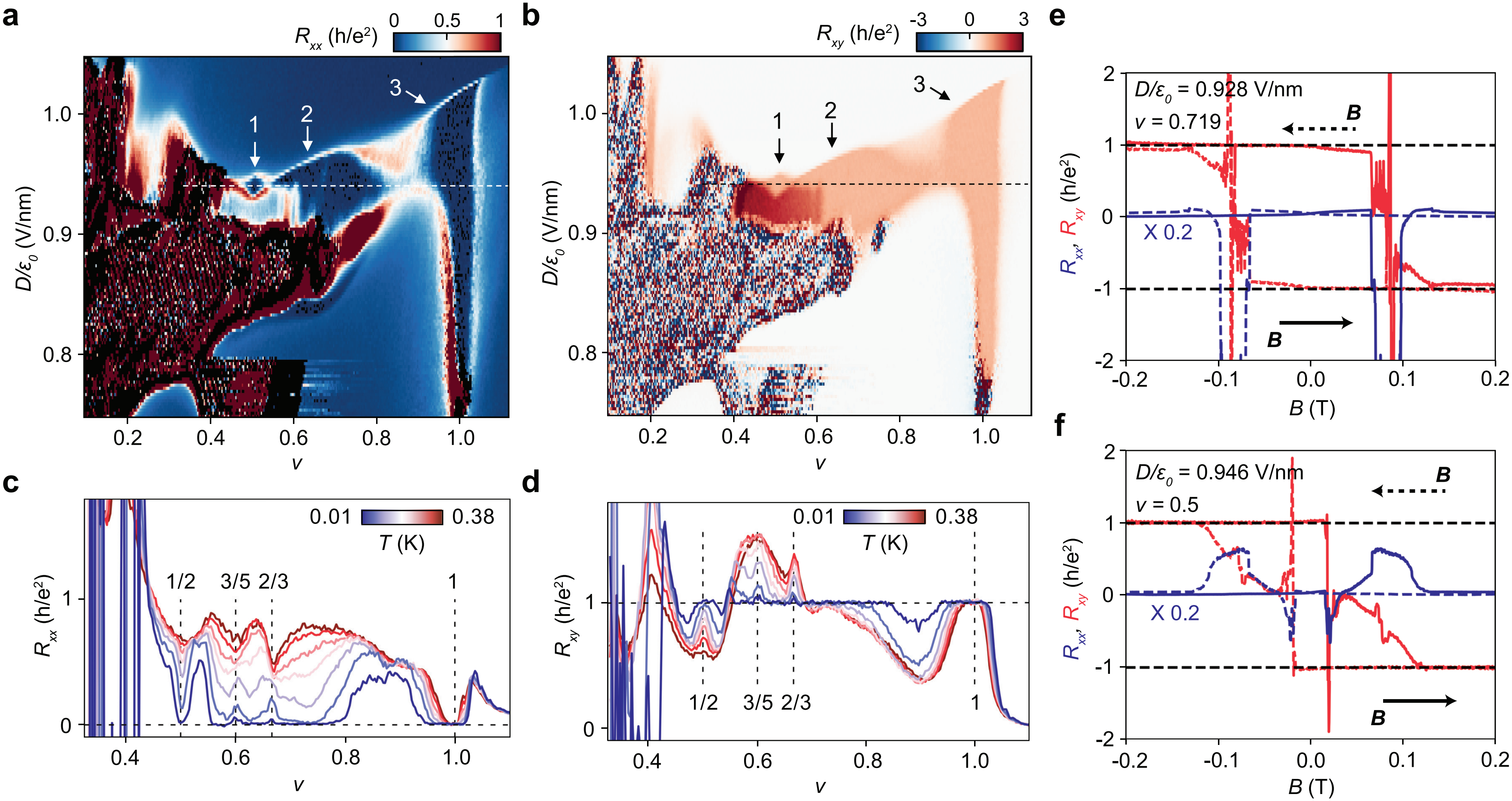
a
R_{xx} (h/e^2)
0
0.5
1
1
2
3
D/ε_0 (V/nm)
1.0
0.9
0.8
0.2
0.4
0.6
0.8
1.0
ν
b
R_{xy} (h/e^2)
-3
0
3
1
2
3
D/ε_0 (V/nm)
1.0
0.9
0.8
0.2
0.4
0.6
0.8
1.0
ν
c
R_{xx} (h/e^2)
0.01
0.38
T (K)
1/2
3/5
2/3
1
1
0
0.4
0.6
0.8
1.0
ν
d
R_{xy} (h/e^2)
0.01
0.38
T (K)
1/2
3/5
2/3
1
1
0
0.4
0.6
0.8
1.0
ν
e
D/ε_0 = 0.928 V/nm
ν = 0.719
B
B
X 0.2
R_{xx}, R_{xy} (h/e^2)
2
1
0
-1
-2
-0.2
-0.1
0.0
0.1
0.2
B (T)
f
D/ε_0 = 0.946 V/nm
ν = 0.5
B
B
X 0.2
R_{xx}, R_{xy} (h/e^2)
2
1
0
-1
-2
-0.2
-0.1
0.0
0.1
0.2
B (T)

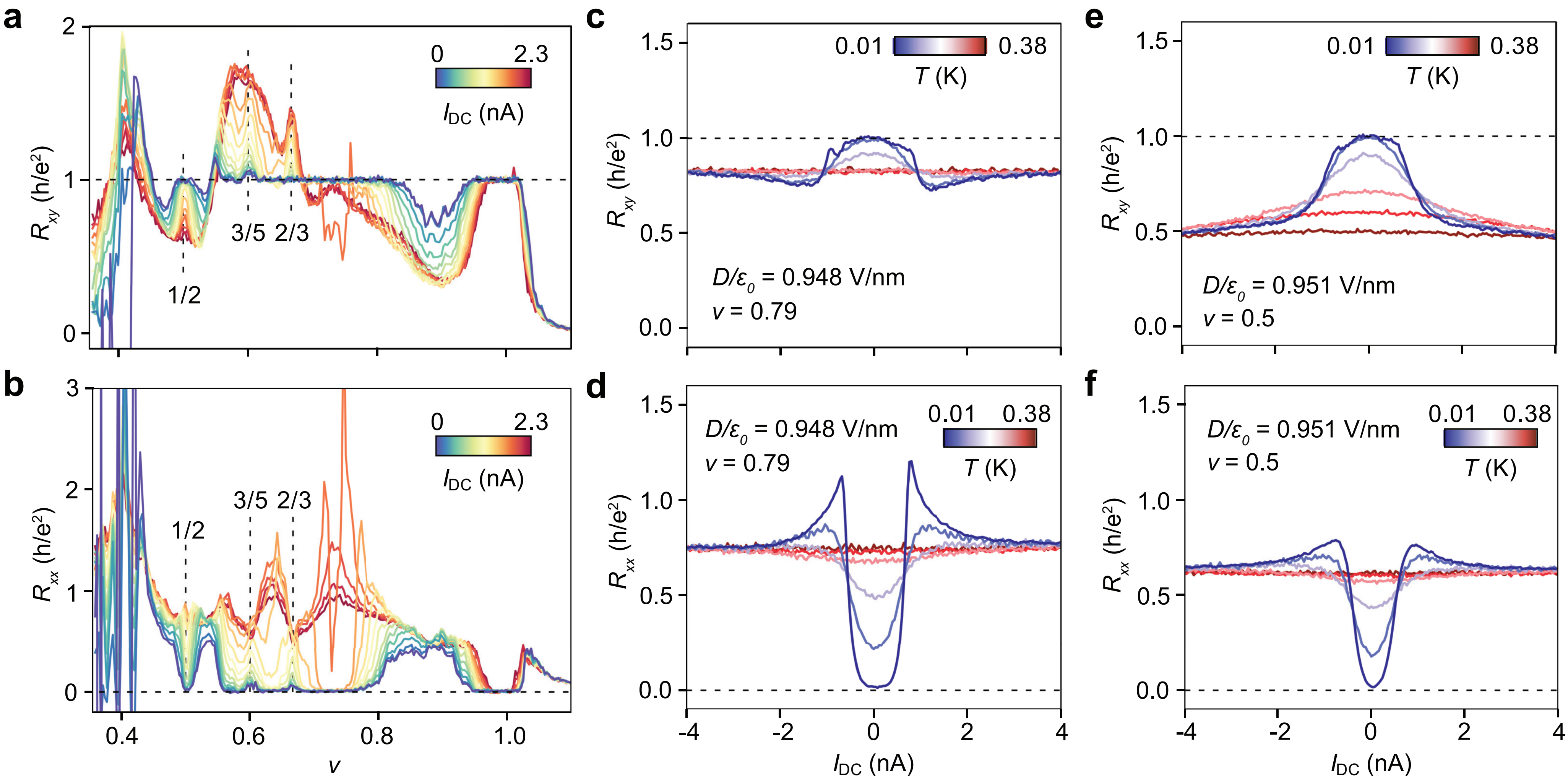
a
b
c
d
e
f
R_{xy} (h/e^2)
R_{xx} (h/e^2)
0
2.3
I_{DC} (nA)
1/2
3/5
2/3
0.4
0.6
0.8
1.0
ν
0.01
0.38
T (K)
D/ε_0 = 0.948 V/nm
ν = 0.79
D/ε_0 = 0.951 V/nm
ν = 0.5
-4
-2
0
2
4
I_{DC} (nA)
0.0
0.5
1.0
1.5
0
1
2
3

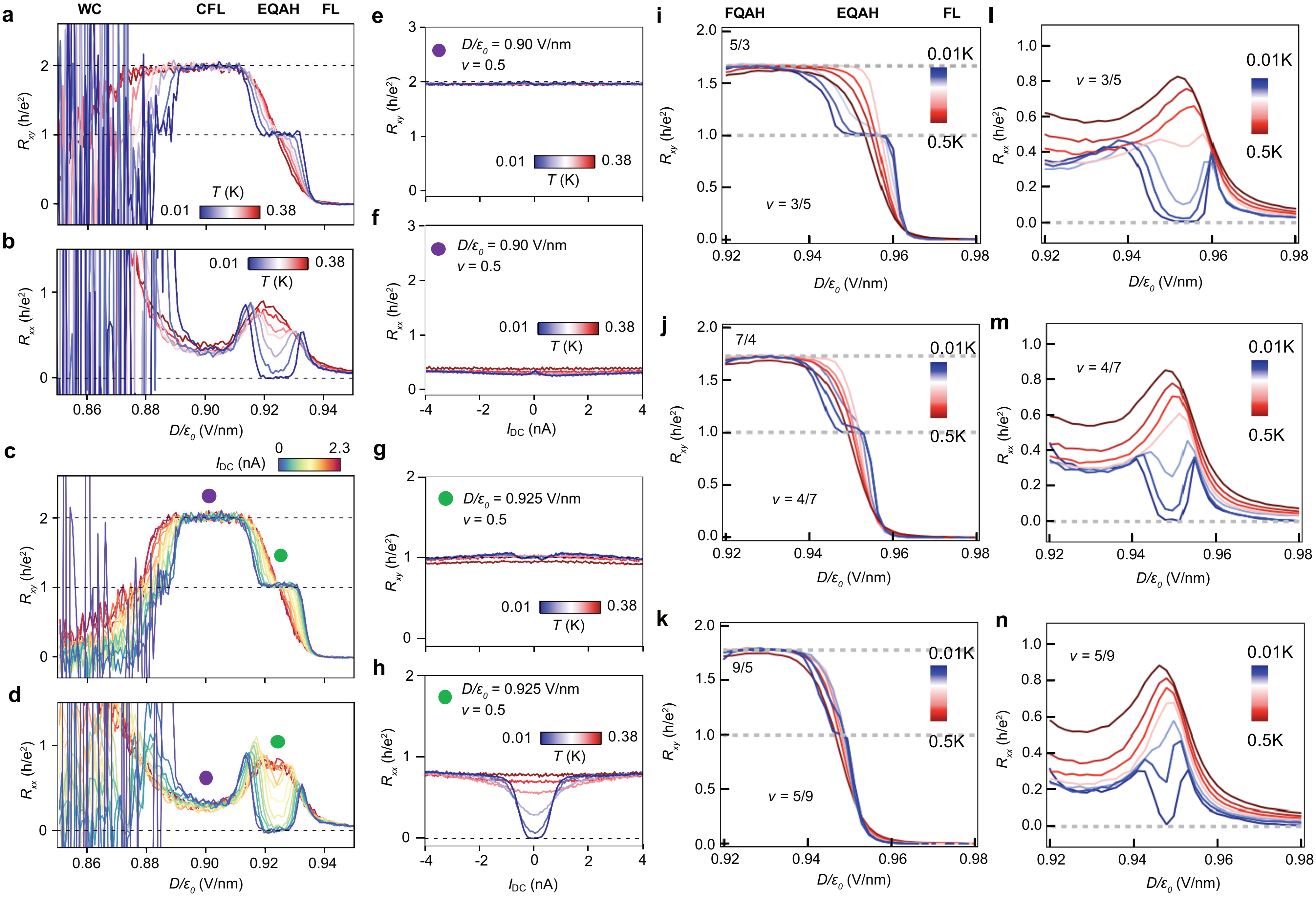

a
WC
CFL
EQAH
FL
R_{xy} (h/e^2)
T (K)
0.01
0.38
b
R_{xx} (h/e^2)
0.01
0.38
T (K)
0.86
0.88
0.90
0.92
0.94
D/ε_0 (V/nm)
c
I_{DC} (nA)
0
2.3
R_{xy} (h/e^2)
d
R_{xx} (h/e^2)
D/ε_0 (V/nm)
e
D/ε_0 = 0.90 V/nm
v = 0.5
R_{xy} (h/e^2)
0.01
0.38
T (K)
f
D/ε_0 = 0.90 V/nm
v = 0.5
R_{xx} (h/e^2)
0.01
0.38
T (K)
I_{DC} (nA)
g
D/ε_0 = 0.925 V/nm
v = 0.5
R_{xy} (h/e^2)
0.01
0.38
T (K)
h
D/ε_0 = 0.925 V/nm
v = 0.5
R_{xx} (h/e^2)
0.01
0.38
T (K)
I_{DC} (nA)
i
FQAH
EQAH
FL
5/3
0.01K
0.5K
v = 3/5
R_{xy} (h/e^2)
D/ε_0 (V/nm)
l
v = 3/5
0.01K
0.5K
R_{xx} (h/e^2)
D/ε_0 (V/nm)
j
7/4
0.01K
0.5K
v = 4/7
R_{xy} (h/e^2)
D/ε_0 (V/nm)
m
v = 4/7
0.01K
0.5K
R_{xx} (h/e^2)
D/ε_0 (V/nm)
k
9/5
0.01K
0.5K
v = 5/9
R_{xy} (h/e^2)
D/ε_0 (V/nm)
n
v = 5/9
0.01K
0.5K
R_{xx} (h/e^2)
D/ε_0 (V/nm)
0.92
0.94
0.96
0.98